Nuclear Inst. and Methods in Physics Research, A 1011 (2021) 165571

Contents lists available at ScienceDirect

Nuclear Inst. and Methods in Physics Research, A

journal homepage: www.elsevier.com/locate/nima

Data-driven simulation of transient fields in air–coil magnets for accelerators

Stefano Sorti [a,b,*], Carlo Petrone [a], Stephan Russenschuck [a], Francesco Braghin [b]

[a] CERN, European Organization for Nuclear Research, CH-1211, Geneva 23, Switzerland
[b] Politecnico di Milano, Dipartimento di Meccanica, via La Masa 1, 20156 Milano, Italy

ARTICLE INFO

Keywords:
Magnetic measurements
Normal-conducting magnets
Dynamic modelling
Model-order reduction
Eddy currents

ABSTRACT

Time-varying fields in fast-ramping magnets for accelerators are difficult to compute in the range of accuracy required for magnet operation. This is due to the complexity of the dynamic phenomena such as hysteresis and 3D eddy currents. On the other hand, magnetic measurements that intercept all these physical phenomena are often limited to a subset of excitation cycles and restricted spatial domains. The measurement results are therefore difficult to extrapolate without a validated physical model of the device.

This paper proposes measurement-updated field simulations to characterize dynamic effects in accelerator magnets. The main idea is to construct a reduced-order model, whose variables are retrievable from measurements by means of a state estimator, and to update the model by minimizing the error between simulations and measurements. The proposed method is applied to a linear, time-transient electromagnetic-field problem of an air–coil corrector magnet with aluminium collars. The proposed method is a first step towards a *hybrid twin* of an accelerator magnet.

1. Introduction

Particle accelerators rely on electromagnets for deflecting and focusing the particle beams. Different designs of magnets are adopted to specific needs, featuring a variety of materials, geometries, and dimensions. The main distinction is the working principle of their excitation coil: iron-dominated normal-conducting magnets, and coil-dominated superconducting magnets [1]. In this paper, we use the example of a coil-dominated, normal-conducting dipole magnet in an aluminium support structure.

Normal-conducting magnets are the first choice when fast ramp rates of the field are required. Therefore, magnets at the injection and extraction points of the accelerator are mostly normal-conducting magnets operated in pulsed mode. Pulsed magnets are also used for energy saving reasons, by reducing ohmic losses [2].

In pulsed magnets, the applied current cycle consists of a series of ramps and plateaus. Ideally, the magnetic field level in the aperture should follow the excitation current with a constant transfer function. But when eddy currents are induced in parts of the magnet, the field level is delayed with respect to the current [3]. This delay depends on the ramp rate, the conductivity, and magnetic permeability of the materials, as well as the geometrical shape of the conductors, collars, and yokes.

The uncertainties in the simulation of transient electromagnetic fields are often larger than the requirements for the beam operation. Reasons include intrinsic errors in model assumptions, approximation errors by the finite-element discretization, and coupled phenomena such as thermal and mechanical effects (magnetostriction).

If a detailed knowledge of the magnet dynamics is required, magnetic measurements are generally the preferred option, as it is possible to measure time-transient phenomena with a relative uncertainty of the order of 10^{-4} [4]. However, measurements are limited by systematic errors (e.g., the calibration accuracy) and random errors (noise). Without an underlying numerical model of the device, it is difficult to interpolate between different excitation cycles or to extrapolate a measurement to higher ramp-rates and current levels.[1]

In this paper we propose a hybrid technique, where a data-driven update is applied to a numerical model of the magnet. The result guarantees reliable extrapolation due to the physical significance of the model, as well as accurate interpolation by matching the measured data.

We consider a normal conducting, coil-dominated magnet without iron-magnetization and hysteresis effects, which therefore results in a linear field problem. Nevertheless, techniques presented here, such as the state estimators, have the potential to be extended to non-linear systems. The flowchart of the proposed method is shown in Fig. 1. It is required that the models of the excitation coils and the aluminium yoke are subjected to a model-order reduction before the assembly of the full system targeted to the updating by measurements. A well-suited excitation function is applied both to the simulation and the real

* Corresponding author at: Politecnico di Milano, Dipartimento di Meccanica, via La Masa 1, 20156 Milano, Italy.
E-mail address: stefano.sorti@polimi.it (S. Sorti).

[1] This has proved necessary in a practical case because of limitations of the power converter in the magnetic measurement lab.

https://doi.org/10.1016/j.nima.2021.165571
Received 4 February 2021; Received in revised form 12 June 2021; Accepted 14 June 2021
Available online 22 June 2021

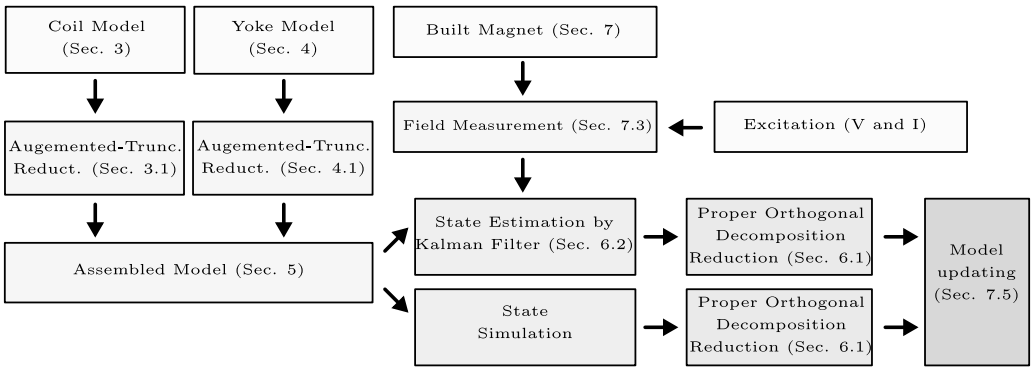

Fig. 1. Flowchart of the proposed technique. Coil and yoke models are reduced by augmented truncation [5]. A Kalman filter is applied to the complete (assembled) model, for the state estimation from measurements and then reduced by proper orthogonal decomposition (POD). In parallel, the response to the complete model is simulated and proper orthogonal decomposition is applied. The two sets of modes are then compared and the model updated.

device in order to model the main dynamics of both. Measurements are processed by a state estimator so that the full state of the system is also available experimentally. The simulated and the measured states are then processed through *Proper Orthogonal Decomposition* (POD) [5] to match the simulated to the measured proper orthogonal modes.

2. Numerical formulation of the field problem

A large number of analytical and numerical methods exist for solving magnetic field problems. The two main families of electromagnetic models are distributed-parameter models and lumped-parameter models, the former are mainly based on finite elements, the latter typically on electrical or magnetic circuit equations [6]. Distributed-parameter models are typically classified as follows:

- In Finite-Element Methods (FEM) the problem is transformed into a weak formulation, and discretized by local basis and shape functions. The method results in sparse matrices, but requires meshing the air region up to the far-field boundaries.
- Boundary-Element Methods (BEM) are based on the Fredholm integral equations, requiring discretization of the domain boundary only. This reduces the number of degrees of freedom of the problem, but the resulting matrices are fully populated and non-linear material parameters are excluded.
- Volume-Integral Methods (VIM) result in less degrees of freedom than the corresponding FEM models, but lead to fully populated matrices.

Hybrid formulations have also been adopted for particle accelerators magnets [1] such as FEM based on reduced vector potentials and coupled FEM/BEM formulations. For our application we apply the VIM formulation because of the following reasons:

- *No meshing of the air domain*. Accelerator magnets are characterized by large air-gaps, in which the field must be determined with the highest possible accuracy. In a FEM domain, a very fine and regular mesh would therefore be required.
- *The excitation field is computed from Biot–Savart type integrals*. This is advantageous for the modelling of the multi-turn coils.
- *The magnetic flux density is a linear function of the updated state variables*. The integral formulations allow to solve directly for the current (and magnetization [7]) distribution in the 3D domain. It is therefore possible to use the same Biot–Savart type integrals for both measurement operation and the source field.

The VIM formulation was first developed for linear conductors [8], and later expanded to include non-linear magnetic materials [7]. Different solutions have been proposed [9] to mitigate the issue of the fully populated matrices; some of them will be discussed in this paper, in particular for the steps preceding the model-order reduction.

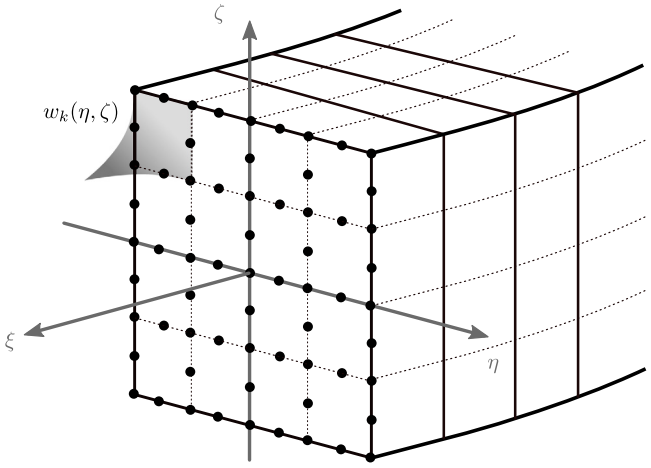

Fig. 2. Discretization of the excitation coil with brick elements. Their local coordinate systems are (ξ,η,ζ). The current-density amplitude is expressed as a function of the shape functions $w_k(\eta,\zeta)$ weighted by $I_{c,k}(t)$.

With respect to the implementation in [8], this paper proposes a slightly different approach where the excitation coils are discretized as line-current segments and the inductance matrices are computed analytically. As the application is a magnet with an aluminium yoke, there is no need to model non-linear ferromagnetic materials. The following sections deal with the main aspects of the model, while details of the numerical implementation are deferred to Appendix.

3. The model for the excitation coil

The multi-turn, 3D geometry of the excitation coil is discretized by a set of brick elements, with a prescribed current direction but varying current amplitude; see Fig. 2. In each cross-section, the Degrees of Freedom (DOFs) are the current densities in the brick. A local coordinate system (ξ,η,ζ) is introduced where ξ is aligned with the normal vector to the cross-section. The direction of the current is expressed by the unit vector $\mathbf{e}_\xi$; thus the current density can be expressed as $\mathbf{J}_c(\eta,\zeta,t) = \sum_k w_k(\eta,\zeta) I_{c,k}(t)\ \mathbf{e}_\xi$. The subscript c denotes all quantities related to the excitation coil.

The discretization of the coil cross section is done according to the expected skin depth δ at the maximum ramp rate, so that all elements in the cross section are smaller than $\delta/2$. Inductance and resistance matrices are assembled by a 2D quadrature rule, which implies that quadrature nodes in the third dimension are along the straight line-current segments.

It is therefore possible to adopt analytical formulas for the mutual inductances, such as Grover's formulas [10], as well as numerical

quadrature techniques based on Neumann's equation [11]. The analytical formulas are more suitable for near interactions, while numerical methods are advantageous for far field interactions, because the computational effort for a given accuracy reduces with the distance. A possible solution to sparsify the matrix, discussed in Appendix A.1, is to perform a state transformation so that the total current in the coil $I_{\mathrm{c,tot}}$ becomes explicitly a degree of freedom. Far interactions can be therefore approximated by considering an equivalent coil segment with $I_{\mathrm{c,tot}}$ instead of the current distribution in the brick elements.

This state transformation also imposes current continuity between the brick elements. The resistance term associated with $I_{\mathrm{c,tot}}$ is the total resistance of the coil, and the self-inductance term is a good approximation of its lumped inductance.

In order to assemble the circuit equation, the minimum energy principle based on Lagrange equations is adopted [12]. This yields

$$[L_{\mathrm{c}}]\frac{\mathrm{d}\boldsymbol{I}_{\mathrm{c}}}{\mathrm{d}t} + [R_{\mathrm{c}}]\boldsymbol{I}_{\mathrm{c}} = \left([M_{\mathrm{c}}] \mid \boldsymbol{P}_{\mathrm{c}}\right)\begin{bmatrix}\boldsymbol{U}_{\mathrm{c}}\\ U\end{bmatrix}, \tag{1}$$

where L_{c} and R_{c} are the inductance and resistance matrices of the coil. On the right-hand side $\boldsymbol{P}_{\mathrm{c}}U$ accounts for the excitation voltage U in the coil, while $[M_{\mathrm{c}}]\boldsymbol{U}_{\mathrm{c}}$ accounts for any other interaction of the conducting domains. The Lagrange approach does not require identifying loops or meshes in the physical circuit. Details on the practical implementation are given in Appendix A.1.

3.1. Model-order reduction of the excitation coil

Model-Order Reduction (MOR) of the excitation-coil model is not strictly necessary for the proposed model-updating, but it is advantageous for this application. Accelerator magnets are designed such that skin effects are small in nominal operation conditions. Reducing the complexity of the full-order coil model allows us to retain the accurate geometrical description of the coil while disregarding the high-frequency response. Reducing the order of sub-systems before assembling the complete model follows the principle of *dynamic substructuring* [13].

The MOR technique is extensively covered in the literature for both linear [5,14] and non-linear systems [15,16]. Because the models presented in this paper do not involve non-linear magnetic materials, linear MOR techniques can be adopted. The equation governing the dynamics of a linear system is written in the time domain as:

$$\dot{\boldsymbol{x}} = [A]\boldsymbol{x} + [B]\boldsymbol{u}, \tag{2}$$

where $\boldsymbol{x}$ is the vector of state variables, $[A]$ is the state matrix, $\boldsymbol{u}$ is the input vector, and $[B]$ is the input matrix. The objective of linear MOR is to establish a transformation $\boldsymbol{q} = [T]\boldsymbol{x}$, where the full-order state of the system is $\boldsymbol{x} \in \mathbb{R}^n$ and the reduced one $\boldsymbol{q} \in \mathbb{R}^m$, with $m \ll n$.

The resulting linear equation systems (both in the frequency and time domains) can be reduced with well established techniques, such as balanced truncation or moment matching [17]. The MOR used for the conductors is known as the *augmented truncation* [5]. A reduced basis is obtained by a proper selection of eigenvectors (modes) of the state matrix. The truncated subset of modes is selected by keeping only the first k modes, up to a given phase shift of the response to the maximum expected frequency $f_{\max}$ in the input. The minimum value for the phase-shift $\phi_{\max}$ is chosen such that all lower-order modes can be considered as static.

The truncated transformation matrix $[T]$ is then augmented by the static contribution of all truncated modes. This allows to recover the behaviour of the full system in static conditions. The only input considered in this process is the voltage from the power supply of the magnet. All modes passing the phase-shift criterion are preserved, regardless of their amplitude.

In order to apply this method to the excitation coil, consider again Eq. (1). The system can be rewritten in the state-space form as

$$\frac{\mathrm{d}\boldsymbol{I}_{\mathrm{c}}}{\mathrm{d}t} = -\underbrace{[L_{\mathrm{c}}]^{-1}[R_{\mathrm{c}}]}_{[A_{\mathrm{c}}]}\boldsymbol{I}_{\mathrm{c}} + \underbrace{[L_{\mathrm{c}}]^{-1}\boldsymbol{P}_{\mathrm{c}}}_{[B_{\mathrm{c}}]}U, \tag{3}$$

where matrix $[A_{\mathrm{c}}]$ is the state matrix. Its eigenvectors are collected in the matrix $[\Psi_{\mathrm{c}}]$ and its eigenvalues are $\boldsymbol{\omega}_{\mathrm{c}}$. The subscript c is kept to distinguish the excitation coil and the contribution from the yoke when the coupled system will be introduced.

It is possible to transform the system equations in modal coordinates by $\boldsymbol{I}_{\mathrm{c}} = [\Psi_{\mathrm{c}}]\boldsymbol{q}_{\mathrm{c}}$. This yields from Eq. (1):

$$\underbrace{[\Psi_{\mathrm{c}}]^{\mathrm{T}}[L_{\mathrm{c}}][\Psi_{\mathrm{c}}]}_{[L_{\mathrm{c}}^{(\mathrm{m})}]}\frac{\mathrm{d}\boldsymbol{q}_{\mathrm{c}}}{\mathrm{d}t} + \underbrace{[\Psi_{\mathrm{c}}]^{\mathrm{T}}[R_{\mathrm{c}}][\Psi_{\mathrm{c}}]}_{[R_{\mathrm{c}}^{(\mathrm{m})}]}\boldsymbol{q}_{\mathrm{c}} = \underbrace{[\Psi_{\mathrm{c}}]^{\mathrm{T}}\boldsymbol{P}_{\mathrm{c}}}_{\boldsymbol{P}_{\mathrm{c}}^{(\mathrm{m})}}U, \tag{4}$$

where subscript (m) denotes modal matrices, which are diagonal because the modes are orthogonal. Modes that exhibit a phase-shift lower than the selected threshold are removed from $[\Psi_{\mathrm{c}}]$, which yields the subset $[\Psi_{\mathrm{c,red}}]$.

The static solution is obtained from the full system, Eq. (1), as $\boldsymbol{I}_{\mathrm{c},0} = [R_{\mathrm{c}}]^{-1}\boldsymbol{P}_{\mathrm{c}}U$. The static response is $\boldsymbol{I}_{\mathrm{c,stat}} = \boldsymbol{I}_{\mathrm{c},0}/U$. It is then possible to compute the vector $[\Psi_{\mathrm{c,stat}}]$ as the residual between $\boldsymbol{I}_{\mathrm{c,stat}}$ and the static response of the reduced system.

The augmented/truncated set of modes is given by $[\overline{\Psi}_{\mathrm{c}}] = ([\Psi_{\mathrm{c,red}}], [\Psi_{\mathrm{c,stat}}])$. Finally, Eq. (4) is re-written with $[\overline{\Psi}_{\mathrm{c}}]$ substituted for $[\Psi_{\mathrm{c}}]$. The resulting reduced matrices are denoted $[L_{\mathrm{c}}^{(\mathrm{r})}]$, $[R_{\mathrm{c}}^{(\mathrm{r})}]$ and $\boldsymbol{P}_{\mathrm{c}}^{(\mathrm{r})}$, where the subscript (r) denotes the reduced order.

4. The model for the conducting yoke

All electrically-conducting domains but the excitation coils themselves, are modelled by the current vector potential formulation ($\boldsymbol{T}$). With $\boldsymbol{J}_{\mathrm{y}} = \nabla \times \boldsymbol{T}$, this yields for the current density $\boldsymbol{J}_{\mathrm{y}}(\boldsymbol{r},t) = \sum_k \nabla \times \mathbf{w}_k(\boldsymbol{r})I_{\mathrm{y},k}(t)$, where $\mathbf{w}_k(\boldsymbol{r})$ are the shape functions of the vector potential and $I_{\mathrm{y},k}(t)$ its line integral along the edge k [8]. The subscript y denotes the variables for the yoke. The choice of current vector potential guarantees that the field solutions are solenoidal. As uniqueness is not guaranteed we apply a tree-cotree gauging. The conducting domain is meshed with hexahedra, supporting Kameari's edge elements [18] with 20 nodes and 36 edge degrees of freedom. The integral equation is given by

$$\eta\boldsymbol{J}_{\mathrm{y}}(\boldsymbol{r},t) + \frac{\mu_0}{4\pi}\int_{\mathscr{V}}\frac{1}{|\boldsymbol{r}-\boldsymbol{r}'|}\frac{\partial\boldsymbol{J}_{\mathrm{y}}(\boldsymbol{r}',t)}{\partial t}\mathrm{dV}' = -\frac{\partial\boldsymbol{A}_e(\boldsymbol{r},t)}{\partial t}, \tag{5}$$

where η is the resistance tensor, μ_0 the vacuum permeability, $\boldsymbol{r}$ the position of the field point and $\boldsymbol{r}'$ of the source point. dV' is the volume element of the source in any conducting domain such as the yoke (or a conducting vacuum chamber). $\boldsymbol{A}_e$ is the magnetic vector potential coupling to the coil or any other source of the magnetic field. Following a Galerkin scheme, the weak formulation results in the linear differential equation system of first order:

$$[L_{\mathrm{y}}]\frac{\mathrm{d}\boldsymbol{I}_{\mathrm{y}}}{\mathrm{d}t} + [R_{\mathrm{y}}]\boldsymbol{I}_{\mathrm{y}} = [M_{\mathrm{y}}]\boldsymbol{U}_{\mathrm{y}}, \tag{6}$$

where $[L_{\mathrm{y}}]$ and $[R_{\mathrm{y}}]$ are the inductance and resistance matrices. $[M_{\mathrm{y}}]\boldsymbol{U}_{\mathrm{y}}$ accounts for the contribution of the vector potential in Eq. (5). More details on the numerical implementation are given in Appendix A.2.

Augmented truncation applied to the yoke takes as an input $\boldsymbol{U}_{\mathrm{y}} = \mathrm{d}\boldsymbol{I}_{\mathrm{c}}/\mathrm{d}t$. It is possible to reduce the excitation of the yoke to a scalar factor; the most trivial approach is to normalize a fixed current distribution in the coil by $I_{\mathrm{c,tot}}$. Applying the Laplace transform to Eq. (6), we obtain

$$s[L_{\mathrm{y}}]\boldsymbol{I}_{\mathrm{y}} + [R_{\mathrm{y}}]\boldsymbol{I}_{\mathrm{y}} = [M_{\mathrm{y}}]\frac{\boldsymbol{I}_{\mathrm{c}}(s_0)}{I_{\mathrm{c,tot}}(s_0)}sI_{\mathrm{c,tot}}(s), \tag{7}$$

where s_0 is the frequency at which the current distribution is computed. It is therefore possible to replicate the augmentation/truncation procedure of Section 3. Eq. (6) is re-written in the state-space form with matrices $[A_{\mathrm{y}}]$ and $[B_{\mathrm{y}}]$. The eigenvectors of $[A_{\mathrm{y}}]$ are collected in the matrix $[\Psi_{\mathrm{y}}]$ and the corresponding eigenvalues are $\boldsymbol{\omega}_{\mathrm{y}}$. The modal coordinate transformation is now $\boldsymbol{I}_{\mathrm{y}} = [\Psi_{\mathrm{y}}]\boldsymbol{q}_{\mathrm{y}}$.

For the evaluation of the modal response at the highest frequency, the current distribution in the coil at $f_{\max}$ is computed. The phase-shift of the yoke modes are evaluated with respect to $I_{\mathrm{c,tot}}$. The static response is given by $\boldsymbol{I}_{\mathrm{y,stat}} = [R_{\mathrm{y}}]^{-1}[M_{\mathrm{y}}]\boldsymbol{I}_{\mathrm{c}}(0)/I_{\mathrm{c,tot}}(0)$. The transformation matrix to obtain the augmented/truncated model is finally given as $\overline{\Psi}_{\mathrm{y}} = ([\Psi_{\mathrm{y,red}}], [\Psi_{\mathrm{y,stat}}])$. The resulting reduced matrices, obtained by applying modal transformation to Eq. (6), are denoted $[L_{\mathrm{y}}^{(\mathrm{r})}]$, $[R_{\mathrm{y}}^{(\mathrm{r})}]$, and $[M_{\mathrm{y}}^{(\mathrm{r})}]$, where the superscript (r) denotes the order reduction.

5. The assembled model

The assembly of the model accounts for the coupling of coil and yoke. Biot–Savart type integrals are again employed; the details are given in Appendix A.3.

5.1. Model assembly

The coupling between the excitation coil and the conducting yoke is performed by computing the matrix $[M_{\mathrm{y}}]$ in Eq. (6), resulting from $\boldsymbol{A}_e(\boldsymbol{r}, t)$ in Eq. (5). The magnetic vector potential is integrated numerically in the yoke domain, by evaluating it in Gauss points by means of the Biot–Savart type integrals. Considering that the coupling is symmetric, a similar computation yields the coupling terms collected in the matrix $[M_{\mathrm{c}}]$ of Eq. (1).

Prior to the final assembly, also this coupling matrix is reduced: $[M_{\mathrm{y,c}}^{(\mathrm{r})}] = [\overline{\Psi}_{\mathrm{y}}]^{\mathrm{T}}[M_{\mathrm{y,c}}][\overline{\Psi}_{\mathrm{c}}]$. The final equation system for the complete magnet assembly is therefore given by

$$\underbrace{\begin{pmatrix} [L_{\mathrm{y}}^{(\mathrm{r})}] & [M_{\mathrm{y,c}}^{(\mathrm{r})}] \\ [M_{\mathrm{y,c}}^{(\mathrm{r})\mathrm{T}}] & [L_{\mathrm{c}}^{(\mathrm{r})}] \end{pmatrix}}_{[L^{(\mathrm{r})}]} \frac{\mathrm{d}\boldsymbol{q}}{\mathrm{d}t} + \underbrace{\begin{pmatrix} [R_{\mathrm{y}}^{(\mathrm{r})}] & 0 \\ 0 & [R_{\mathrm{c}}^{(\mathrm{r})}] \end{pmatrix}}_{[R^{(\mathrm{r})}]} \boldsymbol{q} = \underbrace{\begin{pmatrix} 0 \\ \boldsymbol{P}_{\mathrm{c}}^{(\mathrm{r})} \end{pmatrix}}_{\boldsymbol{P}^{(\mathrm{r})}} U, \tag{8}$$

where the vector $\boldsymbol{q}^{\mathrm{T}} = (\boldsymbol{q}_{\mathrm{y}}, \boldsymbol{q}_{\mathrm{c}})$ contains reduced coordinates of both yoke and coil. The only input of the assembled system is the power supply voltage U and the input vector is $\boldsymbol{P}^{(\mathrm{r})}$.

5.2. Model outputs

The measurable outputs of the model are fluxes or flux-density components, which can be computed with Biot–Savart type integrals for both the excitation coils and the conducting domain. All the (simulated) measurands are collected in the vector $\boldsymbol{y}$. In the most simple case, the magnetic flux density is required in the position of a point-like measurement sensor such as a Hall probe. If induction-coil magnetometers are used, the magnetic flux linkage can be computed by integrating the vector potential along the tracks of the induction coil. Considering that most measurement instruments are based on linear time-invariant equations, it is often possible to write $\boldsymbol{y} = [H]\boldsymbol{q}$ where $[H]$ is a discrete linear operator, mapping a state vector $\boldsymbol{q}$ to measurands $\boldsymbol{y}$.

For model updating by magnetic measurements, the complete model includes the dynamic equation from Eq. (8) and the output equations of the field transducer. Adopting again the state-space representation gives:

$$\begin{cases} \dfrac{\mathrm{d}\boldsymbol{q}}{\mathrm{d}t}(\boldsymbol{q}, t) = [A]\boldsymbol{q}(t) + \boldsymbol{B}U(t) \\ \boldsymbol{y}(\boldsymbol{I}, t) = [H](\boldsymbol{q}, t) + \boldsymbol{n}(t) \end{cases} \tag{9}$$

where $[A] = -[L^{(\mathrm{r})}]^{-1}[R^{(\mathrm{r})}]$ and $\boldsymbol{B} = [L^{(\mathrm{r})}]^{-1}\boldsymbol{P}^{(\mathrm{r})}$ are the state and input matrices.

Remark: Power converters for magnets in particle accelerator are usually current controlled. In order to describe the full electromagnetic behaviour of the magnet, however, the proposed model takes the voltage as input. When a comparison with magnetic measurements is required, it is suggested to not provide the model with the measured closed-loop voltage in feed-forward. A simple control logic (like a P-control with a gain of some units) should be introduced to reduce the error between simulated and measured current.

6. Model updating

Model updating is defined as the process of manipulating a numerical model to minimize the discrepancy between prediction and measurement. While model updating may be limited to adjusting material parameters (such as the conductivity in the aluminium yoke) in the numerical model, we aim not only at minimizing the discrepancy in the numerical simulation, but to derive a physically meaningful model with interpolating and extrapolating properties for a wider range of inputs.

Model updating for linear systems has been extensively studied, particularly in fields of structural mechanics [19–21]. Various approaches deal with models where mass and stiffness matrices are updated after modal transformation, provided that experimental data are available in modal form as well. This is not trivial because measurements often cover only a small fraction of the unknowns in the model. Therefore, it is necessary either to expand the measurements, or to reduce the model, to match the sets of degrees of freedom (DOFs) in the model and measurements. Typically, the missing DOFs are reconstructed from the measured states by the model itself. This techniques is know as coordinate expansion [22].

Limitations in instrument band-width, sensitivity, or sensor positioning may result in missing modes in the measurements, that is, for a model with N degrees of freedom (N modes), only $m < N$ modes may be measured. Different techniques exist to construct updated mass $[M_{\mathrm{U}}]$ and stiffness $[K_{\mathrm{U}}]$ matrices directly from the experimental modes $[\Psi_{\mathrm{X}}]$. For instance, the *matrix-mixing* method [23] proposes the updated matrices as:

$$[M_{\mathrm{U}}]^{-1} = \sum_{i=1}^{m} \boldsymbol{\Psi}_{\mathrm{X},i}\boldsymbol{\Psi}_{\mathrm{X},i}^{\mathrm{T}} + \sum_{i=m+1}^{N} \boldsymbol{\Psi}_{\mathrm{M},i}\boldsymbol{\Psi}_{\mathrm{M},i}^{\mathrm{T}} \tag{10a}$$

$$[K_{\mathrm{U}}]^{-1} = \sum_{i=1}^{m} \frac{\boldsymbol{\Psi}_{\mathrm{X},i}\boldsymbol{\Psi}_{\mathrm{X},i}^{\mathrm{T}}}{\omega_{\mathrm{X},i}} + \sum_{i=m+1}^{N} \frac{\boldsymbol{\Psi}_{\mathrm{M},i}\boldsymbol{\Psi}_{\mathrm{M},i}^{\mathrm{T}}}{\omega_{\mathrm{M},i}}, \tag{10b}$$

where $\boldsymbol{\Psi}_{\mathrm{X},i}$ is the ith column in the experimental mode shape matrix, and $\boldsymbol{\Psi}_{\mathrm{M},i}$ is the ith column of the adjoint set of modes from the model. $\omega_{\mathrm{X},i}$ and $\omega_{\mathrm{M},i}$ are the eigenfrequencies of the experimental and simulated modes.

In order to identify the modes given by measurements and those that must be adjoined, the correlation between the two sets of modes must be evaluated. A learnt method is to compute the Modal Assurance Criterion (MAC) between each $\boldsymbol{\Psi}_{\mathrm{M},i}$ and $\boldsymbol{\Psi}_{\mathrm{X},j}$. This is essentially the normalized scalar product in the n-dimensional space of modes. The closer the MAC is to 1, the higher is the degree of similarity between the modes.

$$\mathrm{MAC}_{i,j} = \frac{\boldsymbol{\Psi}_{\mathrm{M},i} \cdot \boldsymbol{\Psi}_{\mathrm{X},j}}{|\boldsymbol{\Psi}_{\mathrm{M},i}||\boldsymbol{\Psi}_{\mathrm{X},j}|}. \tag{11}$$

Model updating with measured modes requires that they are of limited number and well separated. While in mechanics this is often not an issue [5], electromagnetic modes are less separated. Additionally, they cannot be truncated to less than hundreds of modes, to obtain the required accuracy. The proposed procedure therefore employs a different kind of modes derived from a Proper Orthogonal Decomposition (POD).

The following subsections introduce the concept of POD and its implementation in model updating.

6.1. Proper orthogonal decomposition

Proper Orthogonal Decomposition [24] is a data analysis technique aiming at a low-order approximation of a high-order model. The approximation is expressed by the linear transformation $\boldsymbol{z} = [T]\boldsymbol{x}$, where the high-order model is described by $\boldsymbol{x} \in \mathbb{R}^n$ and the approximation is $\boldsymbol{z} \in \mathbb{R}^m$, where $m \ll n$. This techniques does not require that the model be linear because POD relies on the system response to a prescribed input, by employing selected time-domain snapshots of the response.

Similar to what was done with the state-matrix eigenvectors in Section 3.1, POD allows us to employ the resulting transformation for

model order reduction. However, POD may suffer from a non-optimal choice of the input, while state-matrix modes, that is, the eigenvalues of the state matrix, are input-independent.

The first step of POD is to identify an appropriate input-time sequence, for which the full state of the system is evaluated. The state vectors, called snapshots, are selected at well defined time steps. The result is the matrix of snapshots $[S] \in \mathbb{R}^n \times \mathbb{R}^m$, where n is the dimension of the state vector and m the number of snapshots.

The transformation matrix for model reduction obtained from POD is a subset of the eigenvectors of $[K] = [S][S]^{\mathrm{T}} \in \mathbb{R}^n \times \mathbb{R}^n$. It is possible to drastically reduce the computation time by solving the eigenvalue problem for $[R] = [S]^{\mathrm{T}}[S] \in \mathbb{R}^m \times \mathbb{R}^m$, as $m \ll n$. In this case, the first m modes of $[K]$ are given by

$$\boldsymbol{\Phi}_{\mathrm{K},i} = \frac{1}{\sqrt{\omega_{\mathrm{R},i}}}[S]\,\boldsymbol{\Phi}_{\mathrm{R},i}, \quad i = 1, \dots m. \tag{12}$$

The terms Φ and ω are the eigenvectors and eigenvalues of the matrices in the subscripts. The main drawback of this technique is that, for an ill-conditioned $[S]$ the matrix $[R]$ will be even worse conditioned. The sequence of snapshots must therefore include the most relevant transients, limiting the redundant information.

Proper Orthogonal Modes (POMs), derived from Eq. (12), can be employed in the model-order reduction. The process is similar to Eq. (4), but in this case the resulting matrices are not diagonal: POMs are orthogonal with respect to $[K]$ but not to the state matrix. Consequently, the reduced bases are not independent to each other. Nevertheless, a few POM may provide better performance than a higher number of state-matrix modes [24].

Proper Orthogonal Modes from Eq. (12), can also be computed experimentally, provided that the full state is measured. Incomplete measurements must undergo an expansion procedure before being subjected to POD and updating. In the application presented in the next section, this expansion procedure can be seen as a state estimation, because the only measurable state is the excitation current in the coil.

Once the full state is reconstructed and the POMs computed, also the time history of the POM coordinates can be estimated. $\boldsymbol{z}_{\mathrm{X}} = [\boldsymbol{\Phi}_{\mathrm{X}}]\boldsymbol{q}_{\mathrm{X}}$, where $\boldsymbol{q}_{\mathrm{X}}$ is the vector of the estimated coordinates and $\boldsymbol{z}_{\mathrm{X}}$ the vector of POM coordinates. As long as we refer to POMs as modes, the state-matrix modes are identified with the greek letter $[\Psi]$ (and $\boldsymbol{q}$ for modal coordinates), while the Proper Orthogonal Modes are identified by $[\Phi]$, and $\boldsymbol{z}$ is the set of POM coordinates.

6.2. State estimation

Proper Orthogonal Decomposition requires the full state of the snapshots, thus a Kalman Filter [25] is employed in the reconstruction process. The filter allows us to account for both the noise in measurements (which is already included in Eq. (9)) and the ignorance in the physical model of the magnet. The model in the form of Eq. (9) is thus enriched by adding a disturbance term in the state equation. Disturbances are provided by a vector $\boldsymbol{w}$ of unknown inputs, with a disturbance-input matrix $[\Psi_{\mathrm{m}}]$, which is the matrix of the assembled system modes. In this way, a single covariance is estimated for all elements in $\boldsymbol{w}$ and the disturbances are proportional to the magnitude of each mode. Eq. (9) is adopted for state estimation modifying the first set as:

$$\frac{\mathrm{d}\boldsymbol{q}}{\mathrm{d}t}(\boldsymbol{q}, t) = [A]\boldsymbol{q}(t) + \boldsymbol{B}U(t) + [\Psi_{\mathrm{m}}]\boldsymbol{w}(t)\,. \tag{13}$$

6.3. The updating procedure

The core of the model updating is, as already mentioned, a POD of both the model and the measurements. The same input is applied to the model and the experimental setup, and the snapshots are collected at the same time instant. This yields the matrices of snapshots $[S_{\mathrm{X}}]$ and $[S_{\mathrm{M}}]$.

POMs from the model $\boldsymbol{\Phi}_{\mathrm{M},i}$ and from the expanded measurements $\boldsymbol{\Phi}_{\mathrm{X},j}$ are computed. The indices i and j denote the ith and jth modes of each set. In order to match each of the model and measurement modes, the MAC is computed accordingly to Eq. (11).

Thereafter, the updated matrices can be reconstructed from the experimental modes. Because the POMs form the reduced basis, resuming to the full matrices of physical variables, Eq. (10), is discouraged. The updated model is therefore written directly in a reduced form, approximating the time evolution of the experimentally obtained POM coordinates $\boldsymbol{z}_{\mathrm{X}}$. The starting point is the reduced nonupdated model, derived from Eq. (8):

$$\underbrace{[\boldsymbol{\Phi}_{\mathrm{M}}]^{\mathrm{T}}[L^{(\mathrm{r})}][\boldsymbol{\Phi}_{\mathrm{M}}]}_{[L_{\mathrm{M}}]}\frac{\mathrm{d}\boldsymbol{z}_{\mathrm{M}}}{\mathrm{d}t} + \underbrace{[\boldsymbol{\Phi}_{\mathrm{M}}]^{\mathrm{T}}[R^{(\mathrm{r})}][\boldsymbol{\Phi}_{\mathrm{M}}]}_{[R_{\mathrm{M}}]}\boldsymbol{z}_{\mathrm{M}} = \underbrace{[\boldsymbol{\Phi}_{\mathrm{M}}]^{\mathrm{T}}\boldsymbol{P}^{(\mathrm{r})}}_{\boldsymbol{P}_{\mathrm{M}}}U, \tag{14}$$

where the subscript M denotes the quantities of the numerical model. Assuming that also the experimentally derived POMs evolve according to the same equation, with small updates of the coefficients, it is possible to perform the updating through the coefficients in Eq. (14).

Starting from the nonupdated values, the updated coefficients can be computed by minimizing the vector norm of errors

$$\boldsymbol{e} = \int_{t_0}^{t_1} \left|\boldsymbol{q}_{\mathrm{X}}(t) - \boldsymbol{q}_{\mathrm{M,u}}(t)\right| \mathrm{d}t, \tag{15}$$

where the second term is the result of the numerical model. To reduce the number of unknowns in the procedure, Eq. (14) can be written in state-space form. Some properties of the original matrices, such as symmetry, should be also enforced. The final result of the update procedure is therefore a reduced-order, linear model, describing the behaviour of the POMs that are reconstructed from measurements. The updated model reads:

$$\frac{\mathrm{d}\boldsymbol{z}}{\mathrm{d}t} = [A_{\mathrm{M}}^{(\mathrm{u})}]\boldsymbol{z} + \boldsymbol{B}_{\mathrm{M}}^{(\mathrm{u})}U, \tag{16}$$

where (u) denotes the update and the subscript for $\boldsymbol{z}$ has been omitted to emphasize that this variable is our main quantity of interest. The input U is the voltage across the terminals of the magnet.

7. Experimental validation

To validate the proposed method of data-driven simulation, a measurement campaign was carried out on a dipole magnet, designed for the ELENA accelerator project at CERN [26]. The magnet is built of a pair of saddle-shaped coils that are supported by an aluminium yoke; see Fig. 3(a). The cylindrical bore has a radius of 136 mm and a length of 178 mm. The reference frame, located at the centre of the aperture, is oriented such that x points in the axial direction of the cylinder, y to the top of the magnet, and z in the horizontal direction. The range of the excitation current is 0–45 A and the ramp-rates are between 0 and 400 As^{-1}.

Particle-accelerator magnets are characterized by their Good-Field Regions (GFR), which are the regions of the aperture where the particle beam is supposed to travel. Typically, the required field homogeneity in the GFR is of the order of a few units; the unit defined as $1 \cdot 10^{-4}$ of the main field. The cylindrical GFR in the ELENA magnet is 40 mm in diameter as shown in Fig. 3(b). In this paper, the model updating is performed using the computed and measured field distribution inside the GFR considered as the output of the dynamic system.

The static field in a coil-dominated, normal-conducting magnet can be predicted with high accuracy by applying Biot–Savart's law to the coil field and by limiting discretization error in the numerical model of the contribution by the yoke. Because the ELENA magnet will be operated at very low fields, the yoke is made entirely from aluminium so that iron effects are avoided and no static contribution is expected. In practice, however, coil-dominated magnets exhibit a high sensitivity of the field to coil-positioning errors. As the main objective of the proposed method is to describe dynamic field effects in the magnet, the figure of merit for the updating process, considers only the field errors from the induced eddy-currents. This requires that model errors for static field components be low enough.

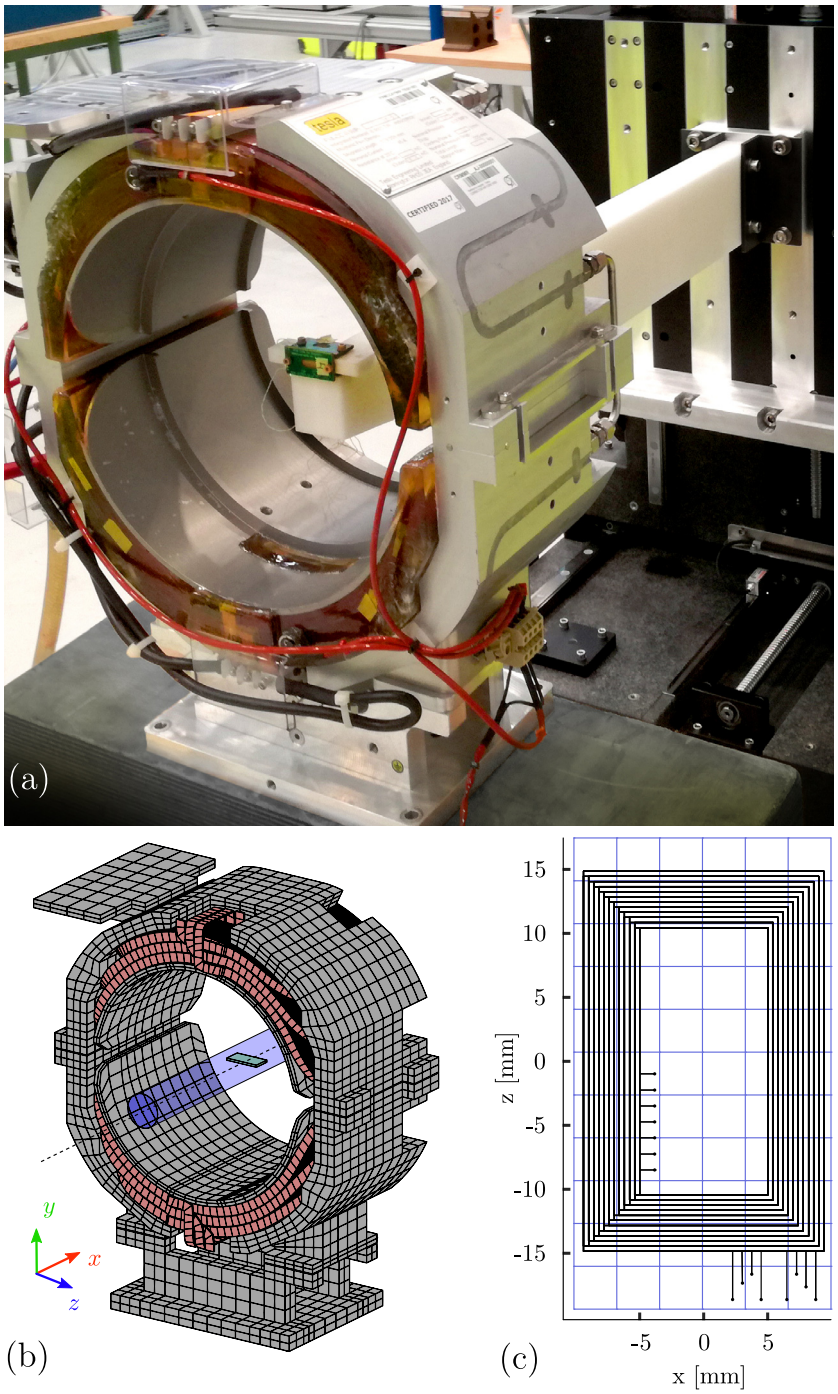

Fig. 3. Experimental validation campaign: the magnet under investigation with the instrument positioned in its centre (a); Model mesh, Good Field Region, reference frame axes orientation (pictured outside of the magnet for clarity) and the main PCB (b); PCB coil track and interpolation grid for the model of measurements, seen from the top (c).

7.1. The experimental set-up

Fig. 3(a) shows a rigid arm holding a set of induction-coil magnetometers in Printed Circuit Board (PCB) technology. The PCB coils are displaced by a 2D precision stage in the magnet bore by ±200 mm along the magnet axis x, and ±20 mm along the vertical y direction. The PCB coil can also be manually adjusted in the z direction, in order to cover the entire GFR.

The field transients due to prescribed excitation-current cycle induce a voltage in the induction coil, acquired at a sampling frequency of 500 kHz by a digital integrator card [27]. The excitation current and the voltage across the magnet excitation coils are also acquired.

In order to exclude thermal effects, the DC resistance of the magnet is monitored such that each measurement can be started with the magnet at the controlled room temperature.

The position of the PCB coil with respect the magnet frame is monitored by a LEICA® laser scanner with a 20 μm accuracy, using retro-reflectors on the magnet, and the PCB. This fiducial marker localization is essential for modelling the measurement set-up by the matrix $[H]$. The relative angle misalignment between the magnet and the measurement instrument resulted in 13.2 mrad for the x axis, 13.0 mrad for the y axis, and 6.1 mrad for the z axis.

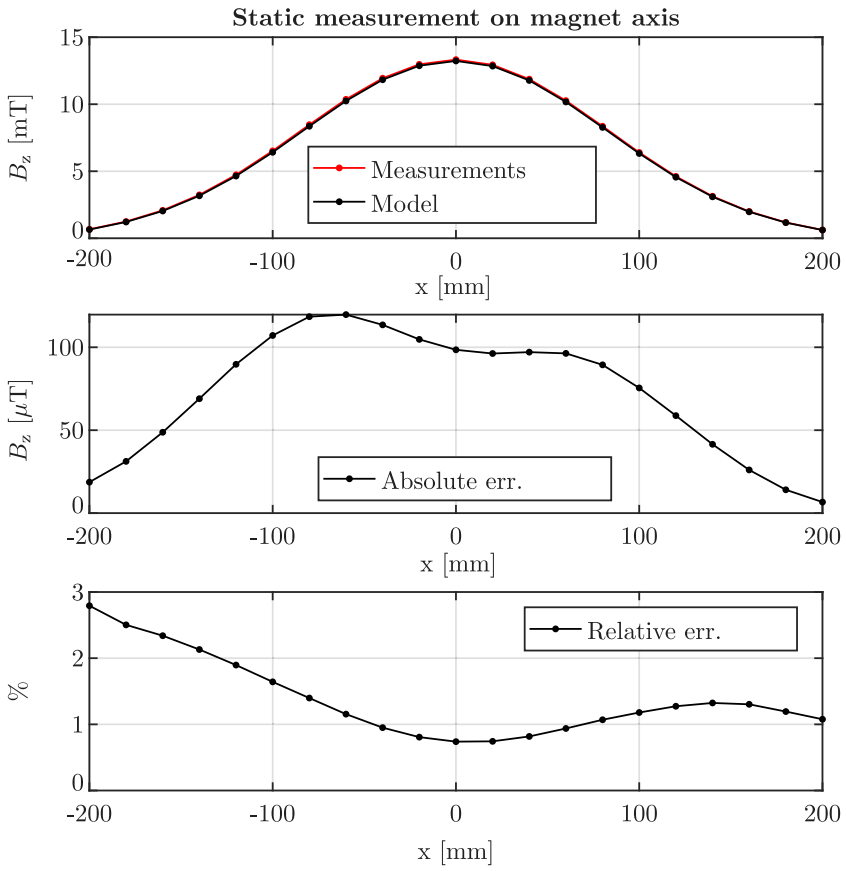

Fig. 4. Static field along the magnet axis. Measurement results are compared to the nonupdated model, through both absolute and relative errors. The flux density is slightly underestimated by the model. Nevertheless, it will be shown that model updating is still applicable for the dynamic effects.

7.2. Model implementation

The modelled magnet geometry is based on design drawings that include small details such as screws and pins, but simplified to guarantee high mesh quality. The meshes for the coil and yoke are shown in Fig. 3(b). The coil is made of about 19000 brick elements with 18 nodes per cross-section. The yoke contains 5800 elements, resulting in a total of 88000 edge shape functions. After gauging, 37500 edges are identified as degrees of freedom. The coil is made of copper (resistivity $\rho_{\mathrm{Cu}} = 16.7\,\mathrm{n\Omega\,m}$), while the yoke is made of aluminium alloy ($\rho_{\mathrm{Al}} = 48\,\mathrm{n\Omega\,m}$). After the coil and the yoke matrices are assembled, each part is reduced by augmented truncation. Eigenvectors of each systems are therefore computed. The eigenvalue problem is solved with the "eig" function in the MATLAB® routines. After augmented truncation, 800 modes are kept for the coil and 2800 for the yoke. The proposed criterion for discarding modes is a phase shift of maximum 5° at 90 Hz, which is the 10-th-order harmonic component of the maximum current ramp cycle, preserving modes with natural frequencies up to about 1700 Hz.

The measurement is simulated by integrating the magnetic vector potential along the PCB coil tracks, whose 3D coordinates are obtained from the design drawing; see Fig. 3(c). Due to the short length of the magnet, it is not possible to identify a truly homogeneous field region and therefore the full 3D geometry of the PCB coil must be considered. This results in thousands of points in which the vector potential, from coil and yoke, must be taken into account. Nevertheless, given that the region occupied by the probe is relatively small with respect to the aperture, it is possible to construct a regular grid around the induction coil and interpolate the vector potential from the grid shown in Fig. 3(c).

In order to guarantee that the result is still a Maxwellian field, harmonic polynomials can be adopted [28]. The original method was developed for the scalar potential ϕ in source-free domains, thus solving $\nabla^2\phi = 0$. For the vector potential under the same conditions, it holds that $\nabla^2 A = 0$ for its three Cartesian components. Convergence is evaluated both in terms of grid size, polynomial orders, and the PCB coil-track discretization. A grid of $10 \times 6 \times 1$ cubes, with a least-square fitting of a 5-th-order harmonic polynomial is chosen for the PCB coil tracks. The flux through the 1400 segments of the PCB coil can be computed with a relative error of less than 10^{-6} with a speed-up by the factor of 100.

The model is a linear time-invariant system, which can be solved both in the continuous-time and discrete-time domains. The magnet model is transformed in a discrete-time system, by a zero-order hold discretization method [29], with time steps matching at least twice the maximum eigenfrequency of the system; in our case this is 0.2 ms.

7.3. Static field components

The first experiment aims at measuring the static magnetic fields for the magnet excited in DC mode. The computed magnet resistance of 0.178 Ω is compared with $R_{\mathrm{c,tot}} = 0.1852\ \Omega$ measured at room temperature (24°C), and the model is tuned accordingly. As shown in Fig. 4, the measured flux density along the magnetic axis is up to 3% higher than in the numerical model.

Different excitation currents are applied to validate the linearity of the field. The transfer function of the flux density in the centre of the magnet for excitation currents from 5 A to 45 A results in $\mathrm{F} = B_z/I = 0.29615\,\mathrm{mT\,A^{-1}}$ with a standard deviation of $\sigma = 18.99\,\mathrm{nT\,A^{-1}}$.

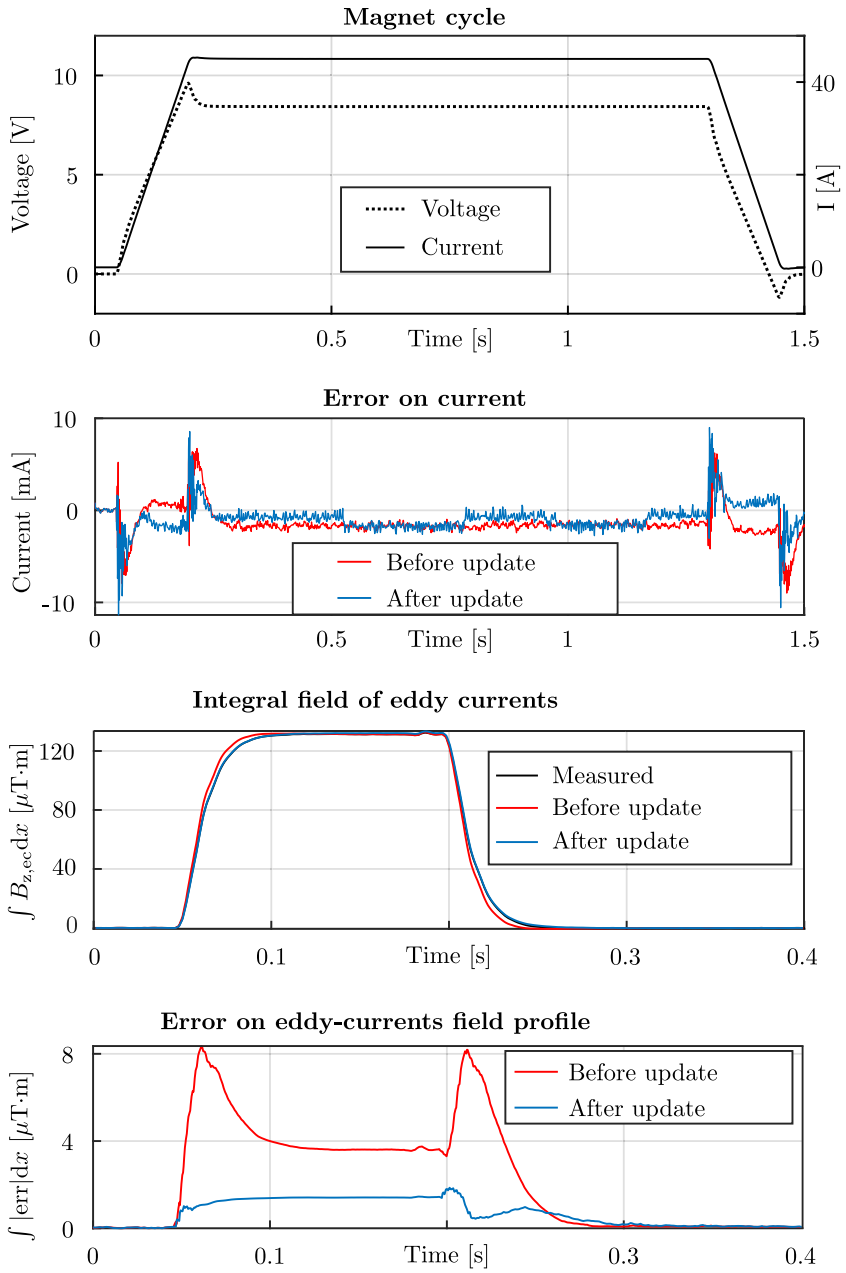

Fig. 5. Measurement of the dynamic field on the magnet axis for the ramp up. From the top to bottom: measured voltage and current for the magnet excitation cycle; POD-reduced model error on current; integral field of eddy currents; integral of flux density error along profile.

7.4. Dynamic fields along the magnet axis

The transfer function of the static field is used to compute the eddy-current field by

$$B_{z,\mathrm{ec}}(x,y,z) = B_z(x,y,z) - \mathrm{F}(x,y,z)\, I, \tag{17}$$

where $B_z(x,y,z)$ and I are the measured quantities. This allows us to identify both the eddy-current transients and the steady-state field distribution. Different current ramp rates are considered to reach 45 A, in order to assess the linearity of the eddy-currents. This step is crucial to ensure that the model updating can be done by measuring only one excitation cycle. Between 100 and 400 $\mathrm{A\,s^{-1}}$, we obtain a central field of 2.24 $\mu\mathrm{T\,s\,A^{-1}}$, with a standard deviation of $\sigma = 6.74$ $\mathrm{nT\,A^{-1}}$. This corresponds to a relative uncertainty of about 0.3% and therefore the eddy-current generation can be assumed to be linear.

Model updating is performed by a set of measurements along the magnet axis for cycles of {0, 45, 0} A at 300 $\mathrm{A\,s^{-1}}$. Field points between −200 mm and +200 mm, with steps of 20 mm are considered. In addition, two measurements at $y = -40$ mm and $y = +40$ mm are taken into account to intercept possible up–down asymmetries in the magnet.

The excitation cycles are repeated 30 times and averaged. The first graph in Fig. 5 is the nominal excitation cycle. The second graph shows the current error in the POD-reduced model before and after updating. The third graph is the integral field generated by the eddy-current distribution:

$$B_{\mathrm{Int}} = \int_{-x_0}^{+x_0} B_{\mathrm{z,ec}}(x)\mathrm{d}x, \tag{18}$$

where $x_0 = 200$ mm. The bottom graph of Fig. 5 are the integrals over the modulus of the error

$$\mathrm{err}(x) = B_{z,\mathrm{ec}}(x) - B^{(\mathrm{m})}_{z,\mathrm{ec}}(x), \tag{19}$$

where (m) denotes the model values (with and without update), while the quantity without superscript is the measured one.

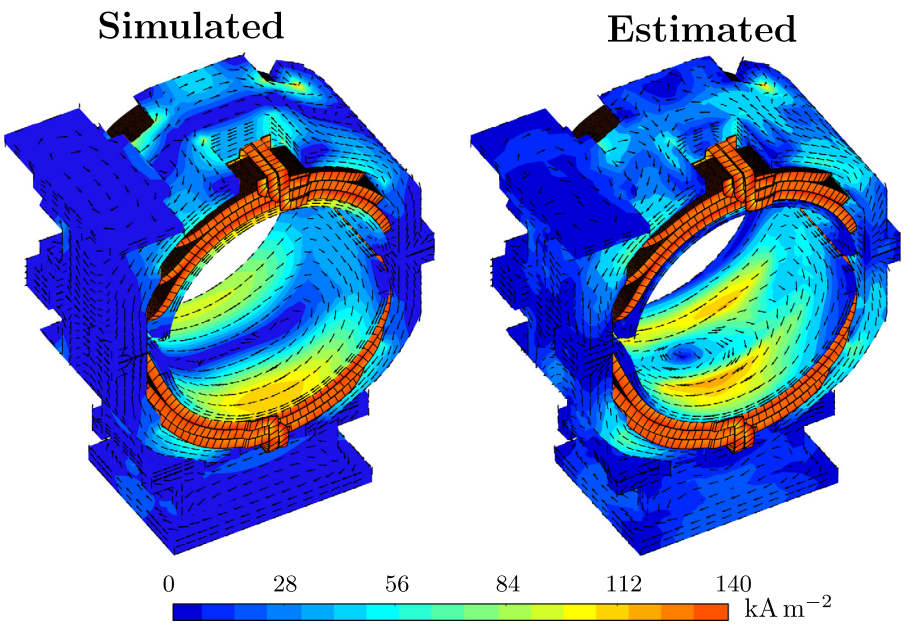

Fig. 6. Eddy-current distribution during ramp-up at $I = 20$ A. The most relevant difference between the simulated and the estimated fields are due to the eddy-currents in the inner shells. This is due to the simplified model not geometrical features in the inner shells. Comparing the model to the real device shown in Fig. 3, reveals that the shell features two protruding edges and therefore the estimated eddy-current distribution can be explained. Moreover the eddy-current distribution in the upper yoke is effected by the safety interlocks and power leads connected in this region.

7.5. Updating the model

The state estimator is implemented in MATLAB® as a discrete time Kalman Filter. The state estimator has to be provided with covariance matrices of the measurement noise, whose amplitudes are estimated to be 100 mA for the current and 10 μT for the flux densities. Different values for model-error disturbances are considered; the best estimation is obtained with $\mathrm{cov}(w_i) = 0.1$.

Voltage and excitation currents are measured together with the magnetic flux density and provided to the state estimator.

Both the model and the state estimator are executed for the nominal current ramp rate of 300 As^{-1}. Fig. 6 shows the eddy-current distributions during the ramp-up, as predicted by the model and as reconstructed by the estimator. The difference in the eddy currents are due to some geometrical features that were neglected in the model; see Fig. 3(a).

For the updating process, three snapshots are taken, so that three POMs can be computed. The snapshots are taken at instances of time of the excitation-current history, shown in Fig. 7. The instances of the snapshots are chosen to capture the main phenomena: steady-state current, steady-state eddy currents, and the transient of eddy currents. The same instances are taken for the model and the state-estimator. Extracting the POM from the snapshots is again an eigenvector problem for the symmetric, positive semi-definite matrix $[R] = [S]^{\mathrm{T}}[S]$. The estimated POM require further processing, as explained in Section 6.1. The time history of the POM coordinates is computed and the coefficients of their dynamic equations are estimated.

The largest POM (z_3) is related to the excitation-coil dynamics, the second (z_2) to the eddy currents in the yoke and the third (z_1) to the eddy currents in the coil; see Fig. 7. Notice that the POM coordinate z_1 represents the time derivative of z_2, and z_2 that of z_3. The MAC matrix between the model POM and the estimated POM resulted in

$$[\mathrm{MAC}] = \begin{bmatrix} 0.2684, & 0.1222, & 0.0024 \\ 0.0811, & 0.8207, & 0.0025 \\ 0.0232, & 0.0015, & 0.9990 \end{bmatrix}. \tag{20}$$

This matrix can be interpreted as follows: before updating, the model of the excitation coil is well describing the coil (z_3), while the main eddy-current distribution in the yoke is less well described (z_2). For this reason, the secondary eddy-currents are poorly represented (z_1). Nevertheless, the matrix is almost diagonal and therefore it is possible to enforce a one-to-one correlation.

The updated values of the coefficients can therefore be computed and provided to the model, mode-by-mode. The final result is a 3-state, linear time-invariant system, where each of the state variables is associated to a current distribution $\boldsymbol{\Phi}_i$. All the computed magnetic fields can be summarized, for the reduced model, in an output matrix of the kind $[C] \in \mathbb{R}^p \times \mathbb{R}^3$, where p is the number of outputs.

The percentage differences between the original and the updated matrices are

$$[E] := 100 \left| 1 - \frac{A_{\mathrm{X},i,j}}{A_{\mathrm{M},i,j}} \right| = \begin{bmatrix} 79.1, & 57.4, & 48.7 \\ 57.4, & 19.6, & 4.78 \\ 48.7, & 4.78, & 7.25 \end{bmatrix}. \tag{21}$$

The POMs that exhibited a lower MAC (z_2 and in particular z_1) are receiving the largest correction. Although the correction for z_1 is relatively large, the weight of this mode in the overall magnet description is only a few percent of the total dynamics.

After model updating with measurements, an additional set of measurements is done for checking the robustness of the method. These measurements include

- Field profiles (inside and outside the GFR) that were not considered in the updating process.
- Different excitation cycles with ramp rates of 400 A s^{-1} and a maximum current level of 35 A (compared to 45 A at 300 A s^{-1} for the updating process).

The quantity of interest is again the integral of the error modulus for the eddy-currents field. Fig. 8 shows the errors as predicted by the nonupdated model and the updated model. Despite higher errors in the 400 A s^{-1} cycle, compared to the nominal 300 A s^{-1} cycle, the updated model is about three times better than the original one in predicting eddy-currents. This performance is preserved even outside the good-field region.

8. Conclusion

This paper presents a first approach in data-driven modelling of normal-conducting magnets for particle accelerators.

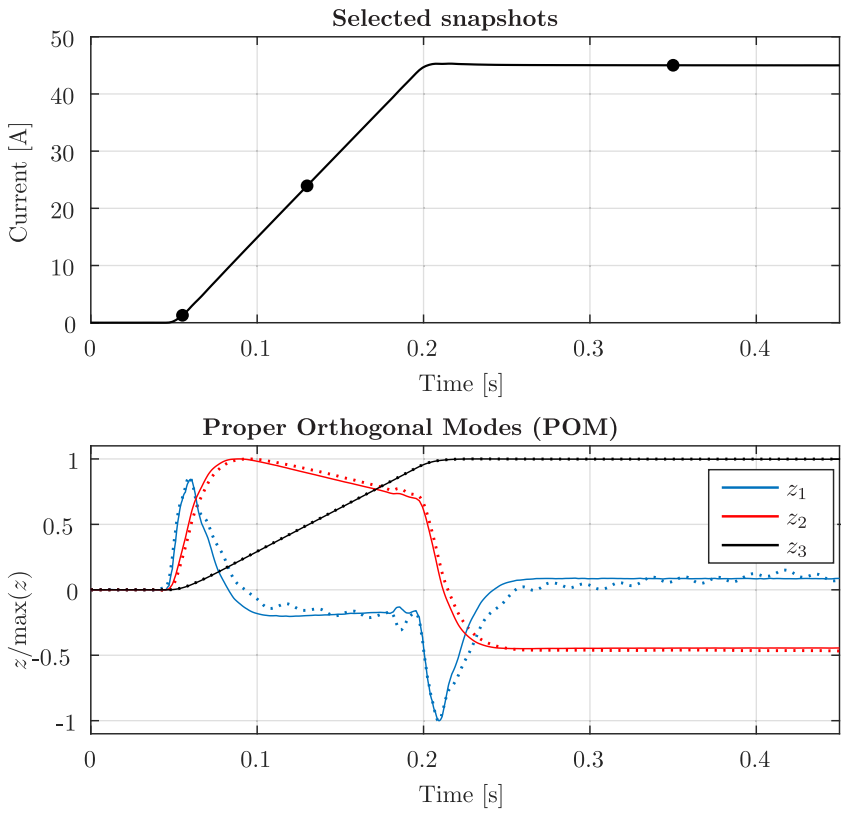

Fig. 7. Selection of snapshots (top) and the normalized POM time history (bottom). Snapshots are taken at three instances of time: (1) eddy-current transient, (2) fully developed eddy-currents, and (3) steady-state. POM (solid line) are derived from the model, dotted lines are estimated.

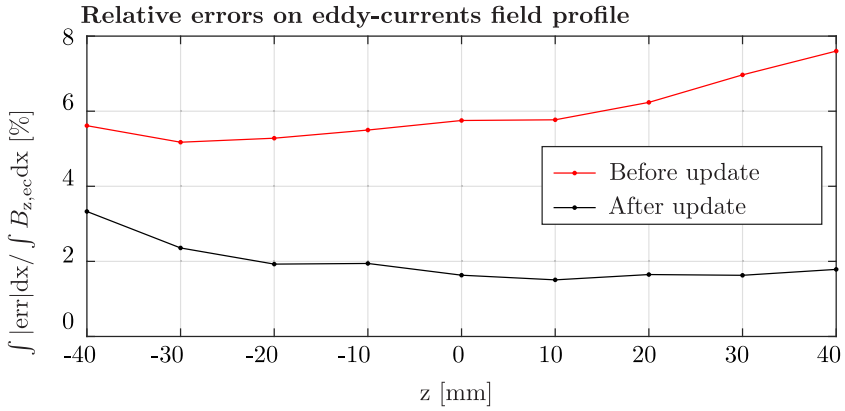

Fig. 8. A comparison between the POD-reduced model before and after updating through a set of measurements.

A Volume Integral Formulation with ad-hoc solutions for excitation coils is implemented. The advantages in using dynamic substructuring, together with modal Model Order Reduction, are highlighted. Proper Orthogonal Decomposition is adopted to further reduce the order of the system and to accommodate corrections based on measurements.

All steps are applied to a coil-dominated dipole magnet built for an accelerator project. The results demonstrate the potential of the proposed techniques, which yield a model of the magnet with only 3 DOFs, but being able to accommodate measurement-driven updates. Experiments have shown an improved accuracy (by a factor of three) with respect the non-updated model.

The most promising aspect of the proposed method is that it is able to cover the whole life cycle of the magnet. The updated model can be used for current cycle optimization or as a diagnostic tool for magnets that are already installed in the accelerator tunnel. The updated model can be seen as a preliminary *digital twin* for the normal-conducting magnet; not only a simulation tool, but also a way to store information during the magnet life cycle.

Future work shall focus on ferromagnetic materials, conceivably including them in the proposed formulation.

CRediT authorship contribution statement

Stefano Sorti: Methodology, Formal analysis, Investigation, Writing - original draft. **Carlo Petrone:** Methodology, Investigation, Resources. **Stephan Russenschuck:** Resources, Supervision, Writing - review & editing. **Francesco Braghin:** Writing - review & editing, Validation, Supervision.

Declaration of competing interest

The authors declare that they have no known competing financial interests or personal relationships that could have appeared to influence the work reported in this paper.

Appendix. The implementation of the electromagnetic model

A.1. The excitation-coil model

As explained in Section 3, the excitation coil is modelled by brick elements with a current-density distribution of fixed direction and variable intensity. Inductances and resistances are therefore computed by a 2D quadrature in the cross-sections of the bricks, resulting in a filament-filament interaction evaluation. The overall procedure for calculating the inductance matrix is given by

$$L_{i,j} = \frac{\mu_0}{4\pi} \int_{\mathscr{A}_i} \int_{\mathscr{A}_j} \mathbf{w}_i^{\mathrm{T}} \left[\int \int \frac{\cos(\alpha)}{|\mathbf{x}_i - \mathbf{x}_j|} \mathrm{d}z_i \mathrm{d}z_j \right] \mathbf{w}_j \mathrm{d}a_i \mathrm{d}a_j, \tag{A.1}$$

where $\mathbf{x}_i$, $\mathbf{x}_j$ are the positions of the filaments, α the angle between filament directions and $\mathbf{w}_i$, $\mathbf{w}_j$ the vectors of the shape functions.

Computing mutual inductances results in a fully populated matrix. The proposed solution is based on the total current

$$I_{\mathrm{tot}} = \int_{\mathscr{A}} J(\boldsymbol{r}) \mathrm{d}a. \tag{A.2}$$

in the cross section and a coordinate transformation so that the n DOFs of a cross-section become the $n-1$ nodal variables, plus I_{tot} that imposes current continuity across the brick elements.

This transformation leads to a sparsification of the inductance matrix. Near interactions are computed between brick elements, while for far interactions line-current segments of I_{tot} are sufficient. The criterion to identify these regions is based on the relative error of these approximation; see Fig. A.9.

The main idea underlying the concepts proposed in Fig. A.9 is that different equations are employed for the calculation of mutual interactions between filaments, depending on the relative distance. In particular, near interactions (region 1) are computed by the Grover's formula [10]. Middle-range interactions (region 2) and far interactions (region 3) are computed with different quadrature points by Neumann's formula [11]. This last equation is used also to express the interactions, outside region 3, directly from the I_{tot} term. The main criterion to identify the region is distance-based: a threshold ϵ is introduced for the relative error between interactions computed with two different formulas. When the error is below the given threshold, the less-accurate but faster method is adopted.

In the case that all the bricks have almost the same length, this evaluation could be done on a sample of interactions. In this way, the regions of application of the various formula are fixed and they can be directly imposed to the segments in the final computation of inductance. These regions are represented in Fig. A.9 as cylinders.

Instead of enforcing Kirchhoff's laws on currents and voltages of the resulting circuit, an energetic approach based on Lagrange equations is adopted [12]: The Lagrangian function is defined as $\mathcal{L} = T - V$, where T and V are the kinetic and potential energies of the system. The mechanical–electrical analogy is presented in Table A.1 It is therefore possible to write:

$$\frac{\mathrm{d}}{\mathrm{d}t} \frac{\partial \mathcal{L}}{\partial \dot{q}_i} - \frac{\partial \mathcal{L}}{\partial q_i} + \frac{\partial D}{\partial \dot{q}_i} = F \quad \text{for } i = 1, \dots, n. \tag{A.3}$$

where q_i are the independent variables of the system. The resulting equation can be written as Eq. (6).

Table A.1
Mechanic–electric analogy for Lagrange equations, for a simple circuit made of a resistor R, an inductor L, and a capacitor Q. k and c are a lumped stiffness and a lumped damper attached to a body of mass m.

Mechanics	Electrics	E mech.	E elec.
Position x	Charge Q	$V = \frac{1}{2}kx^2$	$V = \frac{1}{2}\frac{Q^2}{C}$
Velocity $\dot{x}$	Current I	$T = \frac{1}{2}m\dot{x}^2$	$T = \frac{1}{2}LI^2$
		$D = \frac{1}{2}c\dot{x}^2$	$D = \frac{1}{2}RI^2$
Force F	emf V	$W = Fx$	$W = VQ$

A.2. The conductor model

Eq. (5) is integrated over the volume where $\boldsymbol{J}(\boldsymbol{r}, t)$ is evaluated, where V is the volume element of the source in the domain $\mathscr{V}$. The final equations, as already expressed in Eq. (6), can be written as

$$[L]\frac{\mathrm{d}\boldsymbol{I}}{\mathrm{d}t} + [R]\boldsymbol{I} = \boldsymbol{U}, \tag{A.4}$$

where:

$$L_{ik} = \frac{\mu_0}{4\pi} \int_{\mathscr{V}} \int_{\mathscr{V}} \frac{\nabla \times \mathbf{w}_i(\boldsymbol{r}) \cdot \nabla \times \mathbf{w}_k(\boldsymbol{r}')}{|\boldsymbol{r} - \boldsymbol{r}'|} \mathrm{dV}\mathrm{dV}', \tag{A.5a}$$

$$R_{ik} = \int_{\mathscr{V}} \nabla \times \mathbf{w}_i(\boldsymbol{r}) \cdot \boldsymbol{\eta} \cdot \nabla \times \mathbf{w}_k(\boldsymbol{r}) \mathrm{dV}, \tag{A.5b}$$

$$U_i = -\int_{\mathscr{V}} \nabla \times \mathbf{w}_i(\boldsymbol{r}) \cdot \partial \boldsymbol{A}_e(\boldsymbol{r}, t)/\partial t \ \mathrm{dV}. \tag{A.5c}$$

The self-inductance term becomes singular when source and field points coincide; $\boldsymbol{r} = \boldsymbol{r}'$. Although analytical solutions can be kept finite, numerical methods diverge at this point. To overcome this problem, the equivalent spheres method is adopted [8].

Consistent with learnt practises, tree-cotree gauging is applied. If a tree for the network of edge elements is provided, then the minimum number of unknowns is given by the line integrals of $\boldsymbol{T}$ along the edges forming the corresponding cotree, that is, the degrees of freedom (DOF) associated to the cotree. Every branch of the cotree closes with the tree a loop in which it is the only active edge. Therefore, the value of the line integral of $\boldsymbol{T}$ along the loop is, by virtue of Stokes' theorem, the total current linked with the loop. The potential $\boldsymbol{T}$ is thus uniquely determined for a prescribed solution of the DOF. Imposing that the current density is zero at the domain boundaries implies that the line integral of $\boldsymbol{T}$ is zero as well. Therefore, cotree edges on boundaries of simply connected domains must be excluded.

The inductance matrix is a fully populated matrix. It is symmetric and positive definite, but depending on the geometry, it can be very large, and thus demanding on memory and solution time. A possible mitigation, yet to be fully exploited, is to adopt a low-rank approximation of blocks in the matrix corresponding to far-field interactions. Established methods include domain decomposition, fast-multipole methods or adaptive-cross approximation (ACA) algorithms [31].

A.3. Magnetic field computations

The coupling between the excitation coil and the conducting yoke is given by Eq. (A.5c). The term $\boldsymbol{A}_e(\boldsymbol{r}, t)$ is the magnetic vector potential in the domain of the yoke, generated by the excitation coil. It can be computed analytically with the Biot–Savart law straight line-current segments:

$$\boldsymbol{A}_e = \frac{\mu_0 I}{4\pi} \left[\sinh^{-1} \frac{z_2}{d} - \sinh^{-1} \frac{z_1}{d} \right] \mathbf{e}_{\mathrm{AB}}, \tag{A.6}$$

where I is the current flowing in the segment AB and directed as $\mathbf{e}_{\mathrm{AB}}$, the unit vector in axial direction of the segment. d, z_1, z_2 are geometrical parameters as shown in Fig. A.10a.

The last quantity of interest is the measured magnetic field. Depending on the measurement techniques, $\boldsymbol{H}$, $\boldsymbol{B}$ or $\boldsymbol{A}$ may be required. Their computation must consider the generation from both the exciting

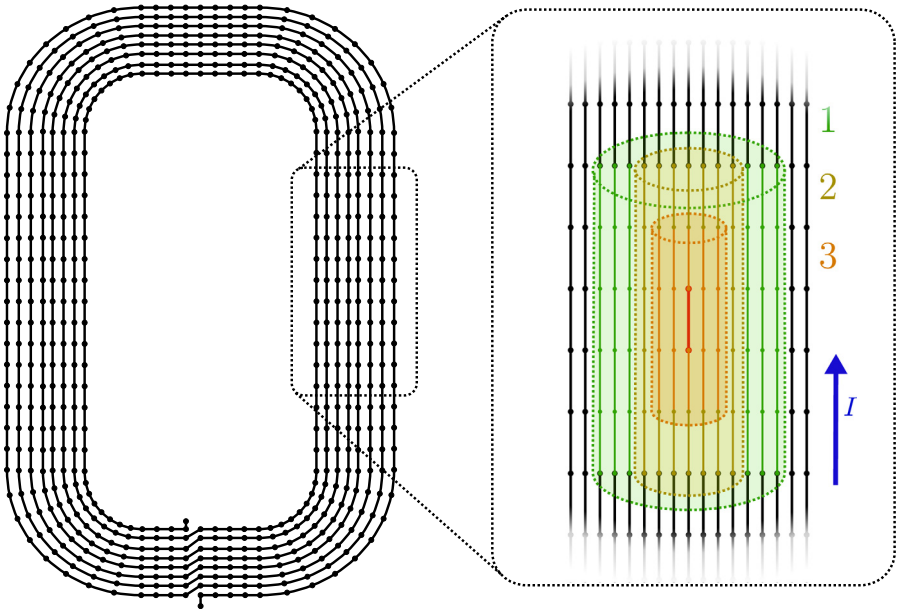

Fig. A.9. Near and far interactions scheme. Different methods for inductance calculation are employed to the three different regions: analytical [10] in region (1), fine numerical quadrature formula [11] for region (2) and reduced numerical [30] for region (3). For brick elements outside these regions, the eddy-current distribution can be neglected and interactions computed by a reduced quadrature method are accumulated in the matrix L related to I_{tot}.

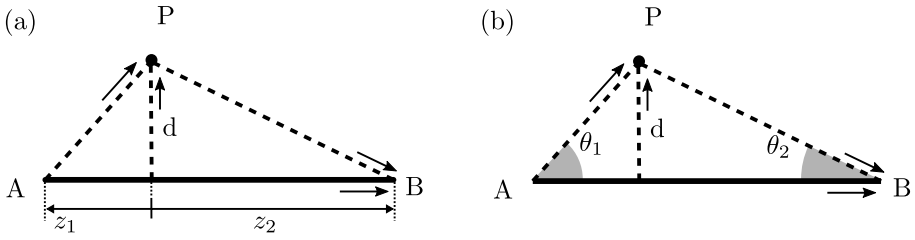

Fig. A.10. Geometric elements and parameters for the computation of $\boldsymbol{A}$ (a) and $\boldsymbol{H}$ (b). Black arrows identify the orientation of segments. Current flows from A to B.

coil and the eddy currents in the yoke. For all the cases, the Biot–Savart law is adopted. As an example, consider the calculation of $\boldsymbol{H}$. As for Eq. (A.6), analytical expressions for finite-length, straight filaments exist, while for solid conductors a numerical integration is required:

$$H_{\text{c}} = \frac{I}{4\pi d}\left(\cos\theta_1 + \cos\theta_2\right), \tag{A.7}$$

$$\boldsymbol{H}_{\text{y}} = \frac{1}{4\pi}\int_{\mathscr{V}} \frac{\boldsymbol{J}(\boldsymbol{r}', t)\times(\boldsymbol{r}-\boldsymbol{r})}{|\boldsymbol{r}-\boldsymbol{r}|^3}\mathrm{dV}' \tag{A.8}$$

The geometric parameters for H_{c} are shown in Fig. A.10b. The direction of H_{c} is orthogonal to the spanned triangle and is determined by the right-hand rule on $\mathbf{e}_{\text{AB}}$.

References

[1] S. Russenschuck, Field Computation for Accelerator Magnets: Analytical and Numerical Methods for Electromagnetic Design and Optimization, Wiley, 2011, http://dx.doi.org/10.1002/9783527635467, URL https://books.google.ch/books?id=tA4VxZvoiJUC.

[2] B. Lamaille, F. Dragoni, S. Evrard, F. Harden, E. Harrouch, M. Lazzaroni, R. Lopez, K. Papastergiou, Study of the energy savings resulting from the East Area renovation, (2019) THPRB087. 3 p, doi: DOI: 10.18429/JACoW-IPAC2019-THPRB087, URL http://cds.cern.ch/record/2692482.

[3] G. Moritz, Eddy currents in accelerator magnets, (arXiv:1103.1800), (2011) 38 p, comments: 38 pages, presented at the CERN Accelerator School CAS 2009: Specialised Course on Magnets, Bruges, 16-25 June 2009. DOI: 10.5170/CERN-2010-004.103. URL http://cds.cern.ch/record/1335027.

[4] L. Bottura, K. Henrichsen, Field measurements, CERN, 2002, http://dx.doi.org/10.5170/CERN-2004-008.118.

[5] B. Besselink, U. Tabak, A. Lutowska, N. van de Wouw, H. Nijmeijer, D. Rixen, M. Hochstenbach, W. Schilders, A comparison of model reduction techniques from structural dynamics, numerical mathematics and systems and control, J. Sound Vib. 332 (19) (2013) 4403–4422, http://dx.doi.org/10.1016/j.jsv.2013.03.025.

[6] M. Yilmaz, P.T. Krein, Capabilities of finite element analysis and magnetic equivalent circuits for electrical machine analysis and design, in: 2008 IEEE Power Electronics Specialists Conference, 2008, pp. 4027-4033. doi:10.1109/PESC.2008.4592584.

[7] R. Albanese, F.I. Hantila, G. Rubinacci, A nonlinear eddy current integral formulation in terms of a two-component current density vector potential, IEEE Trans. Magn. 32 (3) (1996) 784–787, http://dx.doi.org/10.1109/20.497357.

[8] R. Albanese, G. Rubinacci, Integral formulation for 3D eddy-current computation using edge elements, IEE Proceedings A - Physical Science, Measurement and Instrumentation, Management and Education - Reviews 135 (7) (1988) 457–462, http://dx.doi.org/10.1049/ip-a-1.1988.0072.

[9] G. Rubinacci, A. Tamburrino, S. Ventre, F. Villone, A fast 3-d multipole method for eddy-current computation, IEEE Trans. Magn. 40 (2) (2004) 1290–1293.

[10] F.W. Grover, Inductance Calculations: Working Formulas and Tables, D. Van N ostrand Company, Inc., 1946.

[11] R. Dengler, Self inductance of a wire loop as a curve integral, Adv. Electromagn. 5 (1) (2016) 1–8, http://dx.doi.org/10.7716/aem.v5i1.331.

[12] D. Wells, Application of the Lagrangian equations to electrical circuits, J. Appl. Phys. 9 (5) (1938) 312–320, http://dx.doi.org/10.1063/1.1710422.

[13] D. de Klerk, D.J. Rixen, S. Voormeeren, General framework for dynamic substructuring: history, review and classification of techniques, AIAA J. 46 (5) (2008) 1169–1181, http://dx.doi.org/10.2514/1.33274.

[14] U. Baur, P. Benner, L. Feng, Model order reduction for linear and nonlinear systems: a system-theoretic perspective, Arch. Comput. Methods Eng. 21 (4) (2014) 331–358, http://dx.doi.org/10.1007/s11831-014-9111-2.

[15] D. Klis, S. Burgard, O. Farle, R. Dyczij-Edlinger, A self-adaptive model-order reduction algorithm for nonlinear eddy-current problems based on quadratic–bilinear modeling, IEEE Trans. Magn. 52 (3) (2016) 1–4, http://dx.doi.org/10.1109/TMAG.2015.2487601.

[16] K. Hollaus, J. Schöberl, M. Schöbinger, MSFEM And MOR to minimize the computational costs of nonlinear eddy-current problems in laminated iron cores, IEEE Trans. Magn. 56 (2) (2020) 1–4, http://dx.doi.org/10.1109/TMAG.2019.2954392.

[17] W.H. Schilders, H.A. Van der Vorst, J. Rommes, Model Order Reduction: Theory, Research Aspects and Applications, 13, Springer, 2008.

[18] A. Kameari, Calculation of transient 3D eddy current using edge-elements, IEEE Trans. Magn. 26 (2) (1990) 466–469, http://dx.doi.org/10.1109/20.106354.

[19] A. Berman, E. Nagy, Improvement of a large analytical model using test data, AIAA J. 21 (8) (1983) 1168–1173.

[20] B.N. Datta, Finite-element model updating, eigenstructure assignment and eigenvalue embedding techniques for vibrating systems, Mech. Syst. Signal Process. 16 (1) (2002) 83–96.

[21] B. Datta, Finite element model updating and partial eigenvalue assignment in structural dynamics: recent developments on computational methods, in: Proceedings: 10th International Conference ‘‘Mathematical Modelling and Analysis, 2005, pp. 15–27.

[22] B. Caesar, J. Peter, Direct update of dynamic mathematical models from modal test data, AIAA J. 25 (11) (1987) 1494–1499, http://dx.doi.org/10.2514/3.9810.

[23] J.H. Lim, D.-S. Hwang, D. Sohn, J.-G. Kim, Improving the reliability of the frequency response function through semi-direct finite element model updating, Aerosp. Sci. Technol. 54 (2016) 59–71.

[24] Y. Liang, H. Lee, S. Lim, W. Lin, K. Lee, C. Wu, Proper orthogonal decomposition and its applications—Part i: Theory, J. Sound Vib. 252 (3) (2002) 527–544, http://dx.doi.org/10.1006/jsvi.2001.4041, URL http://www.sciencedirect.com/science/article/pii/S0022460X01940416.

[25] R.F. Stengel, Stochastic Optimal Control: Theory and Application, New York, 1986.

[26] S. Maury, W. Oelert, W. Bartmann, P. Belochitskii, H. Breuker, F. Butin, C. Carli, T. Eriksson, S. Pasinelli, G. Tranquille, ELENA: the extra low energy anti-proton facility at CERN, Hyperfine Interact. 229 (1–3) (2014) 105–115, http://dx.doi.org/10.1007/s10751-014-1067-y.

[27] P. Arpaia, L. Bottura, P. Cimmino, D. Giloteaux, A. Masi, J.G. Perez, G. Spiezia, L. Walckiers, A fast digital integrator for magnetic field measurements at cern, in: 2006 IEEE Instrumentation and Measurement Technology Conference Proceedings, IEEE, 2006, pp. 67–71. doi: 10.1109/IMTC.2006.328175.

[28] J.L. Rodrigo Ramon, Maxwellian Interpolation of Magnetic Field, (Master’s thesis), 2018, URL https://fse.studenttheses.ub.rug.nl/17945/.

[29] G.F. Franklin, J.D. Powell, M.L. Workman, et al., Digital control of dynamic systems, 3, Addison-wesley Reading, MA, 1998.

[30] A. Musing, J. Ekman, J.W. Kolar, Efficient calculation of non-orthogonal partial elements for the peec method, IEEE Trans. Magn. 45 (3) (2009) 1140–1143, http://dx.doi.org/10.1109/TMAG.2009.2012655.

[31] K. Zhao, M.N. Vouvakis, J.-F. Lee, The adaptive cross approximation algorithm for accelerated method of moments computations of EMC problems, IEEE Trans. Electromagn. Compat. 47 (4) (2005) 763–773, http://dx.doi.org/10.1109/TEMC.2005.857898.